Supporting Information:

Highly Thermal Conductive Polymer Chains with Reactive Groups: A Step Towards True Application

Anqi Che, ‡[a,b] Yanyan Wu, ‡[a,b,d] Shaoxin Zhou, ‡[e] Wenxue Xu,[f] Wenlong Jiang, [b] You Lv,[b] Wei Guo,[a,b] Keyu Chi,[g] Qi Sun, [g] Tingting Fu,[a,b] Tingting Xie, [a] Yuan Zhu*[a,b,c] and Xin-gang Liang[f]

[a]School of Microelectronics, Southern University of Science and Technology, Shenzhen 518055, Guangdong, China

[b]School of Innovation and Entrepreneurship, Southern University of Science and Technology, Shenzhen 518055, Guangdong, China

[c]Key Laboratory of Energy Conversion and Storage Technologies, Ministry of Education, Southern University of Science and Technology, Shenzhen 518055, Guangdong, China

[d]School of Materials Science and Engineering National Institute for Advanced Materials, Nankai University, Tianjin 300071, China

[e]College of Engineering, Yantai Nanshan University, Yantai 265713, Shandong, China

[f]School of Aerospace Engineering, Tsinghua University, Beijing 100084, China

[g]Foshan (Southern) New Material Research Institute, Foshan 528000, Guangdong, China

Supplementary Note 1. Theoretical calculation

Thermal conductivity: Non-equilibrium molecular dynamics method (NEMD) based on Fourier's Law[1] was used to predict the thermal conductivity of PVA. NEMD requires the use of temperature gradient. The key of NEMD is to apply heat flux or temperature gradient to the system to keep the system in a stable non-equilibrium state[2]. In this paper, the heat flux was obtained by applying a temperature gradient. The two boundary temperatures were set as 320 K and 280 K. Along the heat flux direction, the simulated system was divided into 40 segments, and the local temperature of each segment was then obtained. Based on Fourier's law, the thermal conductivity can be calculated by[3]

$$J = -k\nabla T \tag{S1}$$

$$J = \frac{\Delta E}{A * \Delta t} \tag{S2}$$

$$k = -\frac{\langle J_Z(t) \rangle}{\langle \partial T/\partial Z \rangle} \tag{S3}$$

where J is the heat flux, k is the thermal conductivity, ∇T is the temperature gradient along the direction of the heat flux, A is the cross-sectional area that is perpendicular to the direction of the heat flow, ΔE is the average energy changing value between hot region and cold region during time interval Δt. In this work, the heat flux direction is along the *Z*-axis; $J_Z(t)$ as a function of time t, is the heat flux along the *Z*-axis; $\partial T/\partial Z$ is the temperature gradient along the heat flux direction (*Z*-axis); $\langle\rangle$ means ensemble average.

Orthorhombic and amorphous structures of PVA were established in this work. Figure S1a shows a single PVA chain, which is consisting of C-C backbone and -OH

side chains. Figure S1b and c present chain-aligned crystalline PVA and amorphous PVA. For both crystalline and amorphous structures, the density is set as 0.8 g/cm^3 according to the experiment result, and we set up field force as Consistent Valence Force-Field (CVFF) module[4]. Meanwhile the time step is 0.05 fs. Both non-bond and Coulomb cut-off radiuses are 9.5 Å. Firstly, processes including geometry optimization and annealing were applied in the initial model to obtain the optimal structure in Materials Studio (MS) software. Sufficient NVT relaxation[5] was applied to relax the structure with the thermostat on. In the NVT ensemble, a thermostat was used in the cold and hot regions. Langevin method was used to control temperature[6], until heat flux distribution and temperature were in steady-state. At last, thermal conductivity was calculated by the values of temperature gradient and heat flux.

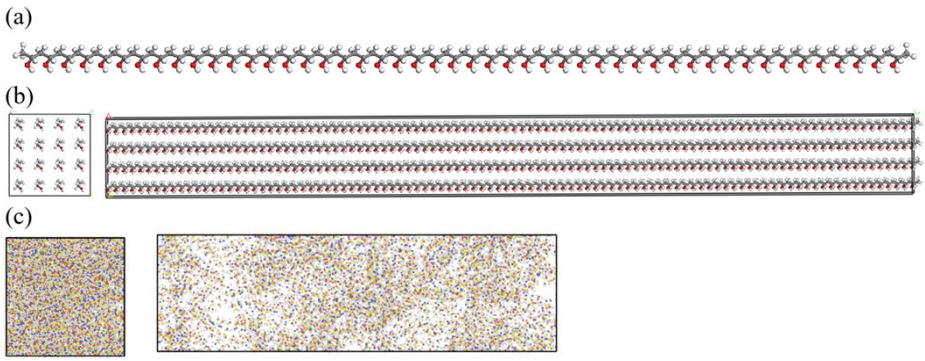

Figure S1 (a) A single PVA chain. (b) Crystalline PVA with aligned chains. (c) Amorphous PVA structure with entangled chains.

Then, for the amorphous PVA, sizes of 27 Å×27 Å×100 Å, 35 Å×35 Å×120 Å, and 46 Å×46 Å×140 Å computing system were created in Amorphous Cell. The calculated thermal conductivity is 0.253 W/m-K.

For the crystalline PVA, the cross-sectional area is 24 Å×24 Å, with system lengths L_Z of 25, 50, 100, and 150 nm in the Z direction created by MS software. Among system lengths, about 10 percent to 15 percent thereof was used as the cold and hot

region as temperature gradient took place in the rest part, while a few atoms at two ends are fixed to form an adiabatic wall. The length of the rest part is the length of calculated chains, which is increased from 19 nm, 20 nm, 76 nm to 116 nm for the investigation of length impact. The calculated thermal conductivity is shown in Fig. 1a&b. The thermal conductivity increases with the increase of chain length in form of[7]

$$k = \frac{1}{3}cvl \qquad (S4)$$

where c is the specific heat of the phonons; v is the phonon group velocity; l is the phonon mean free path. Especially the mean free path l, due to the finite size effect[8], is governed by the relationship $\frac{1}{l} \propto \frac{1}{l_\infty} + \frac{4}{L_Z}$, where l_∞ is the mean free path of an infinite system and L_Z is the length of the system (Z-axis). Then the relationship between k and L_Z is $\frac{1}{k} \propto \frac{1}{l_\infty} + \frac{4}{L_Z}$. As mentioned above, the length of calculated chains (L) is about 80% of L_Z, considering the length loss in the cold region, hot regions, and adiabatic wall. Therefore, the relationship between k and L is $\frac{1}{k} \propto \frac{1}{l_\infty} + \frac{a}{L}$, where a is a constant. The expression ($\frac{1}{k} = 0.574 \times \frac{1}{L} + 0.1178$) shown in Fig. 1 is obtained by fitting the resultant k values from different L inputs (19 nm, 20 nm, 76 nm, 116 nm). The thermal conductivity of infinite length is calculated as 8.49 W/m-K accordingly.

Phonon densities of states (PDOS): Green's function-based molecular dynamics (GFMD)[8] simulation was used to calculate the PDOS of crystalline and amorphous PVA based on the fluctuation-dissipation theory. Green's functions in reciprocal space can be obtained from Fourier transform results of the lattice displacements using molecular dynamics (MD)[9]. Then the force constant matrix and dynamical matrix were

acquired. PDOS was calculated by evaluating the eigenvalues of the dynamical matrix. It is found that this method is capable of yielding the PDOS accurately, since it takes into account the anharmonic effect on phonons simultaneously.

First, different groups of atoms that require phonon analysis were set. In this article, C atom and O atom groups were set in the region without a thermal bath. PDOS of C atom represents atomic vibration modes of the backbone, while PDOS of O atom indicates atomic vibration modes of the side-chains. We used the GFMD method developed by L. Kong et al.[8, 10], which has been embedded into an open-source classical MD simulation code LAMMPS as an extension.

Comparison of PDOS in literatures: In previous computational studies, first-principles calculations and numerical solution of the Boltzmann Transport Equation (BTE) were used to investigate the PDOS of PE[11], and self-consistent density functional perturbation theory (DFPT) were used for the PDOS of PVA[12]. The results are re-depicted in Figure S2 for better comparison.

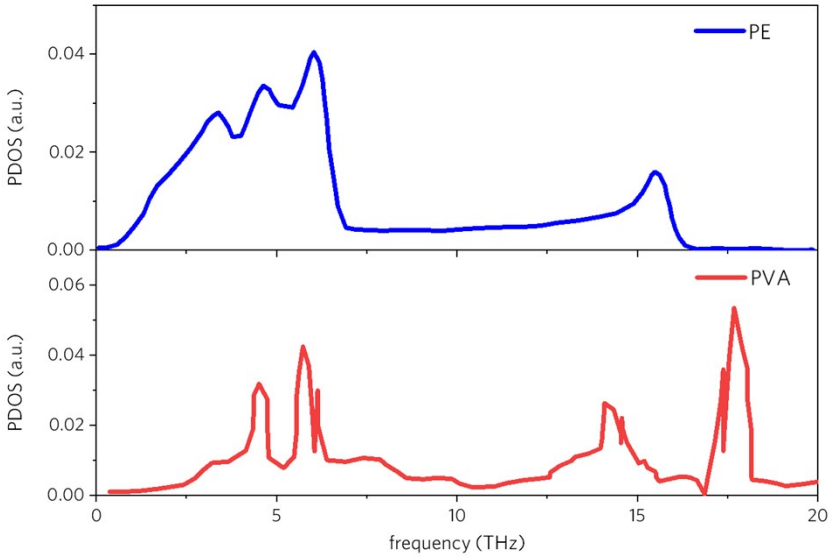

Figure S2 PDOS of bulk PE crystal[11] and bulk PVA crystal[12].

Supplementary Note 2. Fabrication of thermally conductive PVA nanostructured films

Disentangling chains: 10 wt.% PVA (Mw ~145,000, *L*~1000 nm) solution was prepared by dissolving PVA solid particles into pure water, which requires 4 hours stirring at 60 ℃. Ultrasonic vibration (ultrasonic cell crusher 250Y, Bilon) was applied to the solution further to break the intra- and inter- molecular hydrogen bonds and thus reduce the entanglement of PVA chains. The change of the entanglement degree could be sensed by viscosity, which changed drastically from around 5000 cP to around 1000 cP. The solution was used without any further purification. Applying shear force can also help disentangling chains[13,14], yet many bubbles arise in the solution during the shearing process and more time is needed for degassing. Therefore, ultrasonic treatment is chosen in the work.

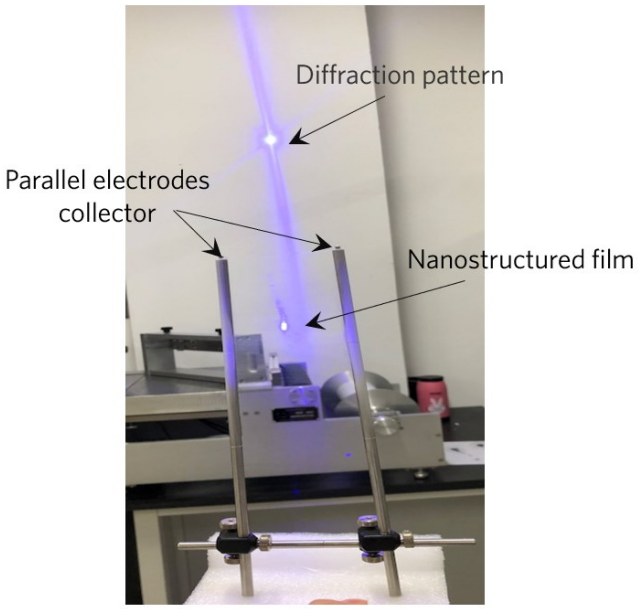

Figure S3 Homemade parallel electrodes collector.

Aligning fibers in the film: Nanostructured film was produced by the electrospinning method. A pair of parallel electrodes collector was set up to obtain highly orientated fibers (Figure S3). The spinneret was connected to the positive pole,

and the collector was connected to the negative pole. The introduction of the parallel electrodes collector (in Figure S4a) determines the configuration of the external electric field and nanofibers driven by the electrostatic force tend to be in alignment.[15] The cross-sectional view of the collector is shown in Figure S4b. In the vicinity of the collectors, the electric field lines are split into two fractions pointing toward opposite edges of the gap between two metal stripes, and the charged nanofibers are mainly driven by the electrostatic force. The electrostatic force is in the same direction as the electric field lines and should pull the two ends of the fiber toward the two electrodes, which eventually results in the high alignment of the fibers across the gap.

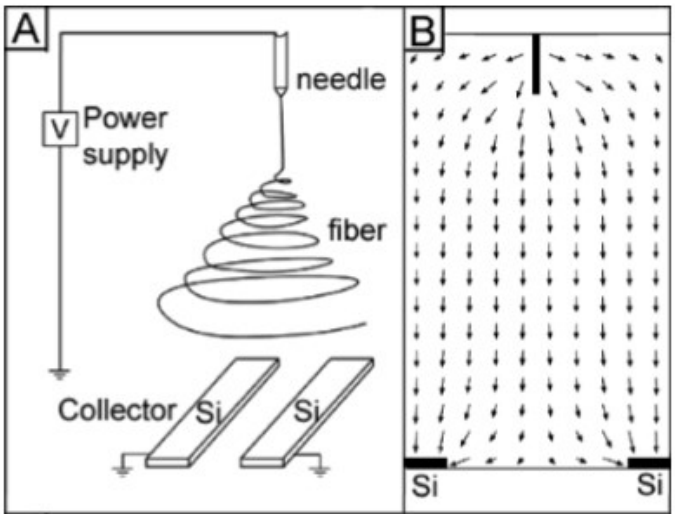

Figure S4 (a) Schematic illustration of the setup for electrospinning with the parallel electrode collector. (b) Calculated electric field strength vectors in the region between the needle and the collector. The arrows denote the direction of the electrostatic field lines

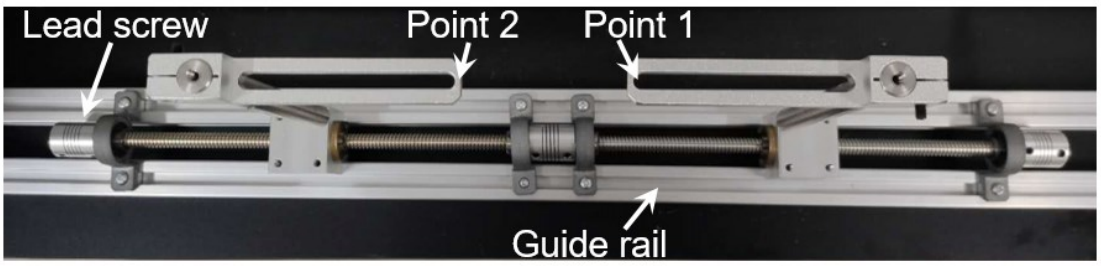

Figure S5 Photo of the homemade uniaxial stretching equipment

Hot Stretching: A homemade uniaxial stretching equipment (Figure S5) with infrared heating chamber (300 W) was used in this work. The two ends of the film are stuck on point 1 and 2 along the guide rail. During the hot-stretching process, the lead screw is adjusted for aligning and stretching the film. The final dimension for the film is 20 cm x 5 cm x 0.1~0.3 mm. The sample in real view is shown in Figure S6. The hot stretching process naturally causes a decrease in the diameter of nanofibers in the nanostructured film. The average diameter changes from ~130 nm of the as-spun sample to ~50 nm (λ=8) (Figure S7a&b). Meanwhile, the nanofiber alignment degree is also enhanced. Figure S7c&d show the Fourier transform of Figure S7a&b. The fiber alignment degree f is calculated accordingly based on Equation S6 and S7.

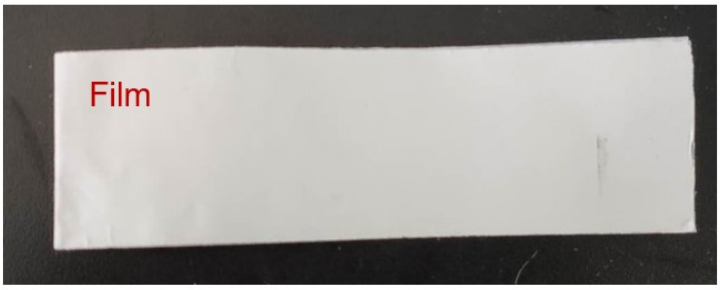

Figure S6 Photo of the sample in real view

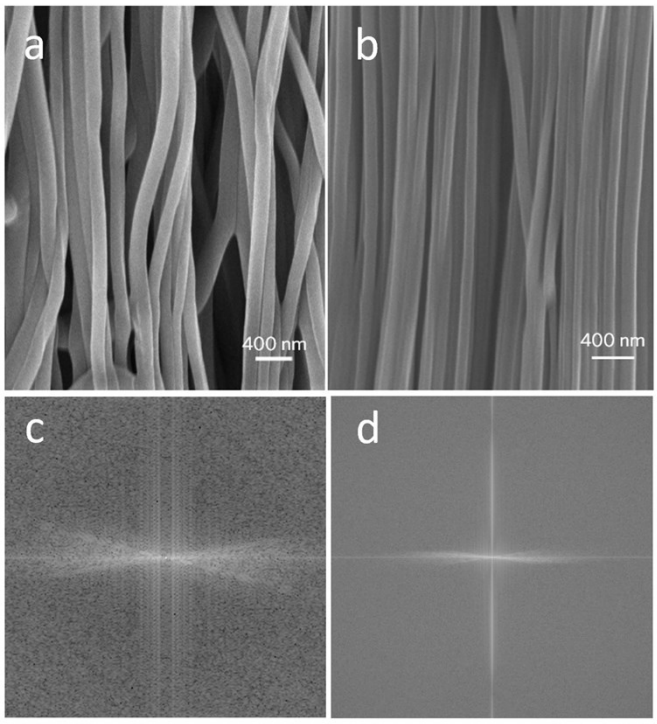

Figure S7 SEM images of the nanostructured film before (a) and after (b) hot stretching (λ=8); (c) and (d) Fourier transform of (a) and (b).

Supplementary Note 3. Alignment measurement

Wide-angle X-ray scattering (WAXS) measurement: WAXS measurements were used to determine the crystallite orientation and crystallinity. The X-ray irradiation is at a wavelength of $\lambda_{CuK\alpha} = 0.154$ nm.

In a WAXS pattern, the crystalline orientational factor is quantified by the orientational distribution function (ODF) P, whose relationship with intensity distribution expression is given by[16]:

$$P = \frac{\int_0^{\pi/2} I(\phi)cos^2\phi d\phi}{\int_0^{\pi/2} I(\phi)d\phi} \qquad (S5)$$

ϕ is the azimuthal angle between the structural unit vector and the reference direction in the WAXS patterns. $I(\phi)$ is the azimuthal intensity profiles obtained by X-ray diffraction measurement.

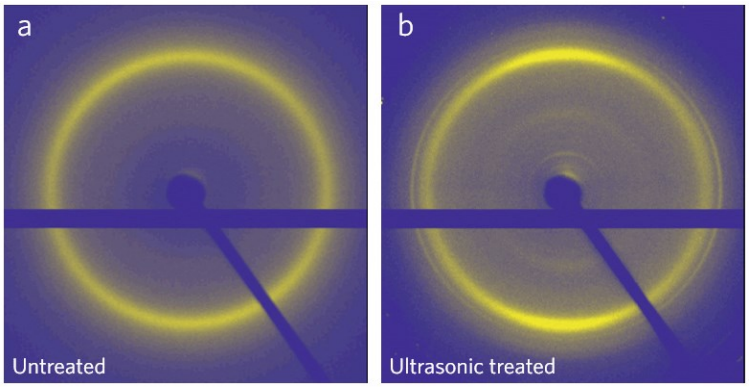

Figure S8 WAXS patterns of (a) entangled chains; (b) disentangled chains.

Polarized FTIR measurement: The FTIR experiments were performed by Fourier transform infrared spectrometer (Nicolet IS50). The range of light wavelength is 2.5 μm~25 μm. The light incident angle is 90 ° to the film.

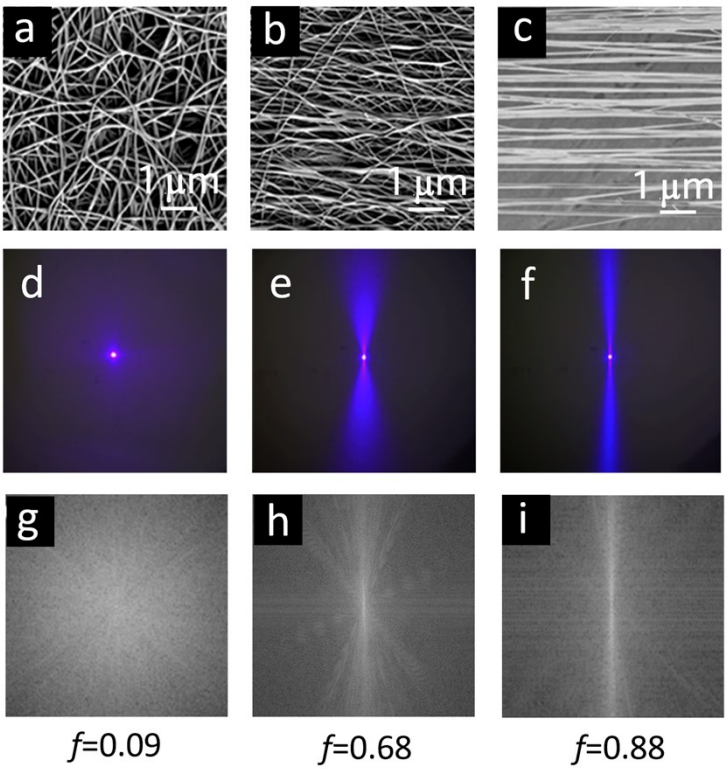

Figure S9 (a, b, c) SEM images; (d, e, f) LD patterns; (g, h, i) Fourier transform of SEM images of nanostructured films with different alignment degree *f* (0.09, 0.68, 0.88). The LD patterns are in very high analogy with the Fourier transform of SEM images.

On-line Laser diffraction method: The diameter of fibers is ~200 nm, thus a blue laser (wavelength 405 nm) was used, and the power was set at 100 mW to avoid film damaging. The laser was placed 10 cm away from the film and the laser beam was nearly perpendicular incident to the film. A black screen was placed on the other side of the film to collect diffraction patterns. The alignment degree *f*, which is also called Herman's Orientation Factor (HOF), can be calculated by the intensity distribution in the diffraction pattern[17]:

$$f = \frac{3\langle cos^2\theta \rangle - 1}{2} \qquad (S6)$$

$$\langle cos^2\theta \rangle = \frac{\int_0^{\pi/2} I(\theta) cos^2\theta sin\theta d\theta}{\int_0^{\pi/2} I(\theta) sin\theta d\theta} \qquad (S7)$$

where θ is the angle between the structural unit vector and the reference direction and $I(\theta)$ is the intensity profile of anisotropy as a function of θ from 0 to π/2 in the laser diffraction patterns or Fourier transform of SEM images.

It is noteworthy that in this work HOF only accounts for the alignment degree of fibers, while ODF accounts for the alignment degree of both fibers and polymer chains.

Supplementary Note 4. Thermal diffusivity measurements

Angstrom method was used for α measurement. In this method, one end of a one-dimensional sample is heated by a thermal wave (Figure S11). When the temperature oscillations stabilize, measurements of the amplitude (*M* and *N*) and phase delay (*dt*) of the temperature oscillations at two spots (at a distance of *L*) along the sample enable calculation of the thermal diffusivity of the sample $(\alpha = \frac{L^2}{2dtln(M/N)})$.

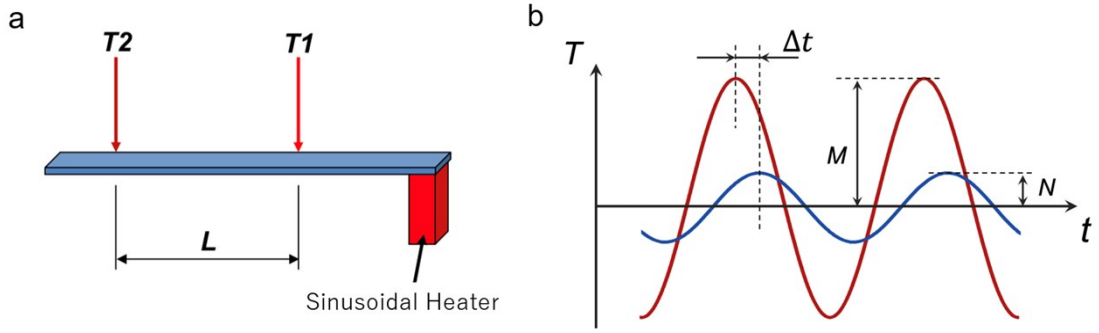

Figure S11 the schematic diagram of the Angstrom method.

Platform set-up: The schematic diagram and the photo of the home-built thermal diffusivity testing system are shown in Figure S12a&b. High-resolution IR camera (PI640, Optris GmbH) is used as the temperature sensor which enables capturing the temperature profile at any spot along with a fiber sample as thin as ~ϕ50 μm. The wire sample is gently stretched taut while placed between the TEC module (heatwave source) and the heat sink. A modified vacuum chamber (Figure S12c) is used to minimize the convectional heat loss. A lid with a small CaF_2 window is placed to seal the chamber for vacuum pumping. The window transmits the mid-wavelength infrared which the IR camera utilizes for temperature sensing.

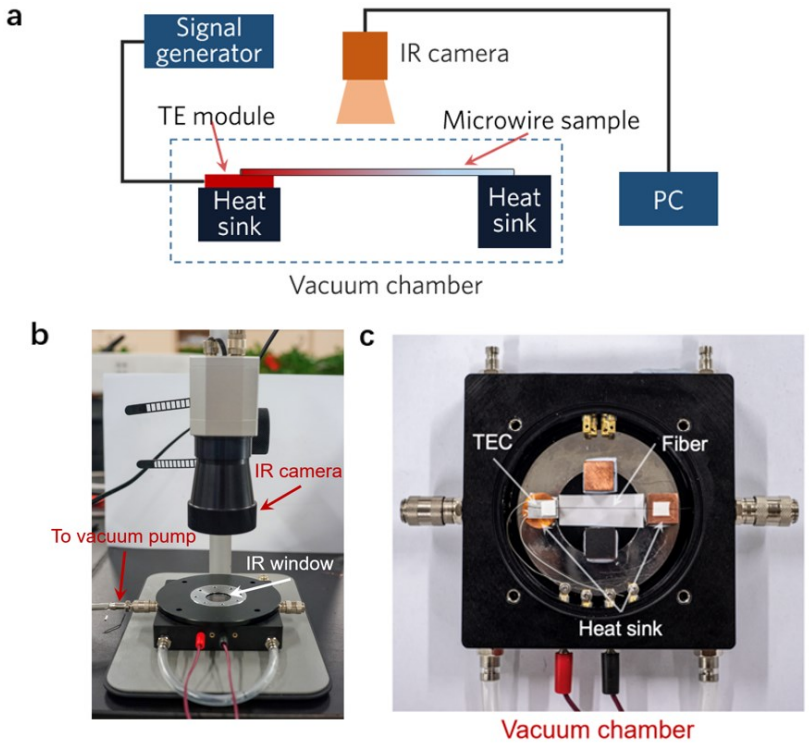

Figure S12 (a) Schematic and (b) Photo of the thermal diffusivity measurement system. (c) Top-view of the vacuum chamber.

Platform calibration: A constantan wire (α =6.1-6.2 mm^2/s diameter 100 μm) was used as the control sample. The IR image of the constantan wire is shown in Figure S8a and the corresponding temperature profiles at different spots are shown in Figure S13. Figure S14a&b are the temperature amplitude and temperature phase plots deduced from Figure S13b. The calculated thermal diffusivities of the constantan wire varying with testing distance are shown in Figure S14, which is stable and very close to the documented value.

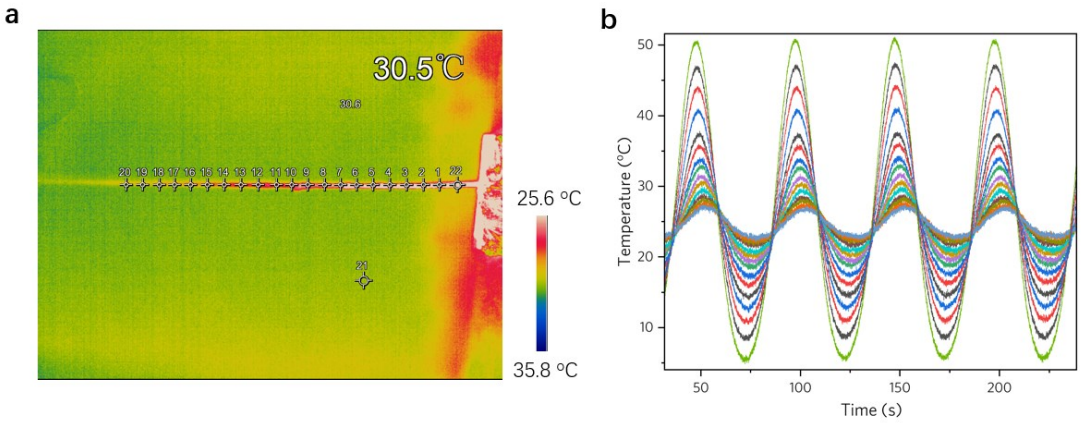

Figure S13 (a) The IR image of the constantan wire under test. (b) Temperature profiles at different spots along the constantan wire.

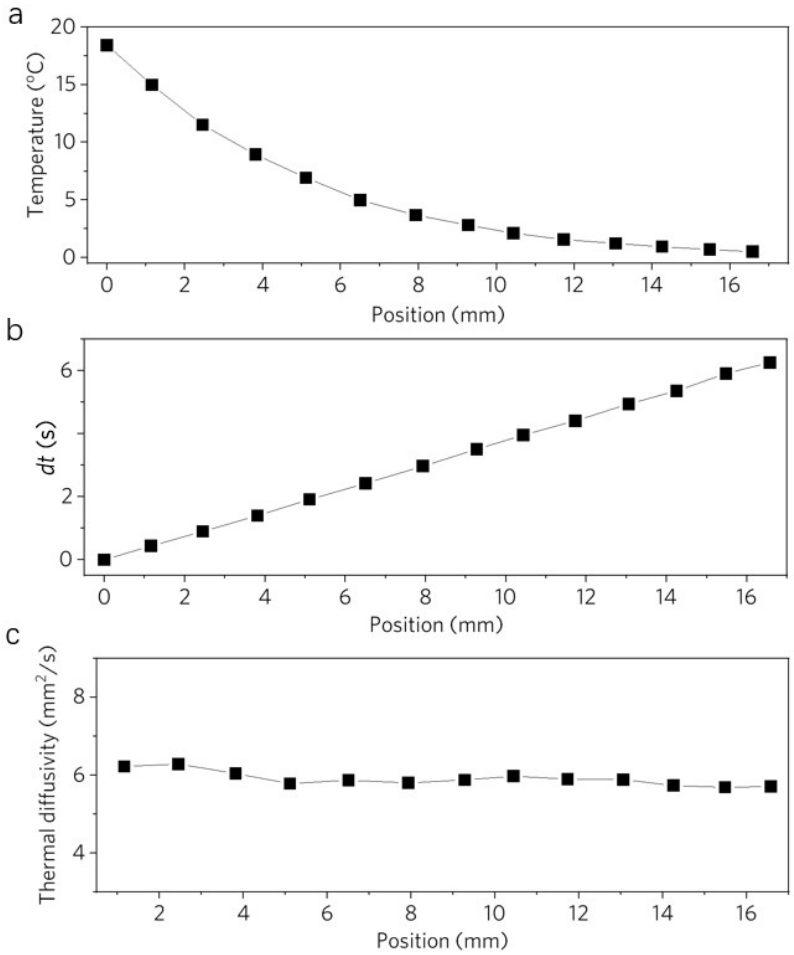

Figure S14 (a) Temperature amplitude, (b) temperature phase and (c) calculated thermal diffusivity at different spots along the constantan wire. The frequency of the temperature oscillation is fixed at 0.04 Hz.

We investigated the impact of temperature amplitude on thermal diffusivity. The measured thermal diffusivity of constantan wire decreases for higher amplitude. The increase of the heat loss induced by high-temperature amplitude may introduce increasing system error and result in a lower apparent diffusivity. Experimentally, we can use extrapolation to minimize the temperature amplitude impact and the intercept at zero amplitude could be taken as the true α value (Figure S15). In this way, the value of α for constantan wire is 6.14 mm^2/s, very close to its documented value (6.1-6.2 mm^2/s).

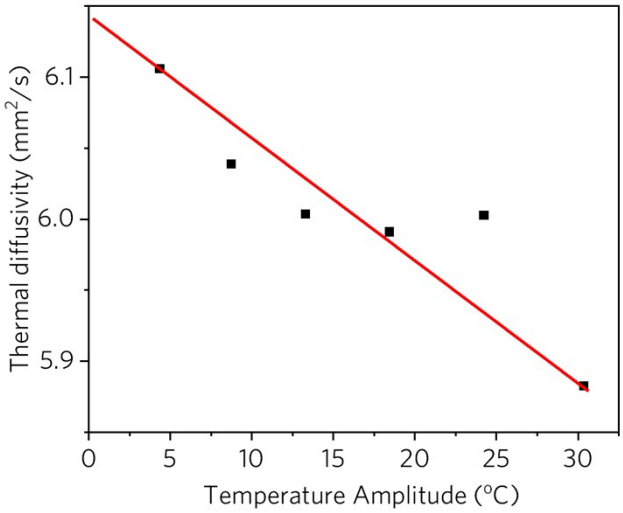

Figure S15 Comparison of the α value in response to temperature amplitude for constantan wire.

Figure S16 compares the thermal conductivities of various samples reported in other works[18-22]. and in this work. All the measured values in this work agree very well with reported ones.

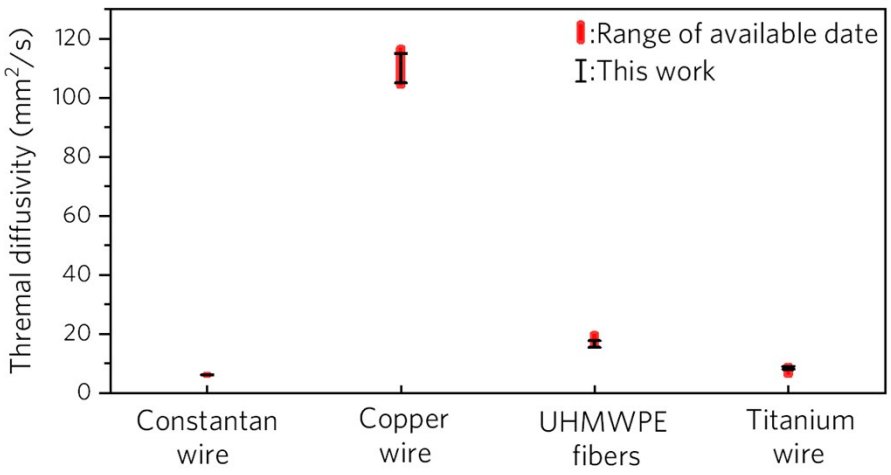

Figure S16 Comparison of the measured and published thermal diffusivity values of various samples.

System uncertainty analysis: The total uncertainty incurred during measurement follows the uncertainty propagation rule[22]

$$(\delta f)^2 = \sum_i \left(\frac{\partial f}{\partial x_i}\right)^2 (\delta x_i)^2 \qquad (S8)$$

where δ means uncertainty and all the x_i are uncorrelated parameters. From the expression $\alpha = \frac{L^2}{2dt \ln \frac{M}{N}}$, the total uncertainty in α is,

$$\delta\alpha = \left[\left(\frac{L}{dt \ln\frac{M}{N}}\delta L\right)^2 + \left(\frac{L^2}{2dt^2 \ln\frac{M}{N}}\delta dt\right)^2 + \left(\frac{L^2}{2dt\frac{M}{N}\ln^2\frac{M}{N}}\delta\frac{M}{N}\right)^2\right]^{1/2} \qquad (S9)$$

and $\delta\frac{M}{N} = \pm\left(\frac{\delta M}{N} + \frac{M}{N^2}\delta N\right)$.

The first term is length origin (denoted as $\delta\alpha_L$), the second term is phase lag origin (denoted as $\delta\alpha_{dt}$) and the third is amplitude origin (denoted as $\delta\alpha_{\frac{M}{N}}$). Here δdt is around 0.031 s derived from the data acquisition frequency 32 Hz. δL is about 0.0168 mm from the pixel resolution of the IR camera. δM and δN are around 0.3 °C derived from the

waveform fitting. Every origin of uncertainties is calculated and listed in Supplementary Table 1. For the case of constantan wire, the uncertainty is mainly contributed by the length origin and the amplitude origin. The total uncertainty shows a minimum zone at moderate L. If L is chosen properly, the uncertainty can be control around 5–6% or at least under 10%.

Table S1 the uncertainties incurred during the measurement of constantan wire.

L (mm)	dt (s)	$\frac{M}{N}$	$\delta\alpha_L$ (mm^2/s)	$\delta\alpha_{dt}$ (mm^2/s)	$\delta\alpha_{\frac{M}{N}}$ (mm^2/s)	$\delta\alpha$ (mm^2/s)	$\frac{\delta\alpha}{\alpha}$
2.45	3.10	1.60	0.23	0.24	0.42	0.54	0.09
3.81	3.60	2.06	0.24	0.16	0.32	0.43	0.07
5.10	4.11	2.66	0.23	0.11	0.27	0.37	0.06
6.50	4.62	3.69	0.22	0.08	0.21	0.31	0.05
7.93	5.17	5.00	0.22	0.07	0.23	0.33	0.06
9.27	5.71	6.52	0.21	0.06	0.26	0.34	0.06
10.43	6.16	8.71	0.21	0.05	0.26	0.34	0.06
11.73	6.61	11.71	0.21	0.04	0.30	0.37	0.06
13.05	7.14	15.07	0.21	0.04	0.37	0.43	0.07
14.25	7.56	19.43	0.21	0.04	0.43	0.48	0.08
15.47	8.11	26.53	0.20	0.03	0.45	0.49	0.09
16.57	8.46	35.64	0.20	0.03	0.57	0.60	0.10

Supplementary Note 5. Discussion on Differential scanning calorimetry (DSC)

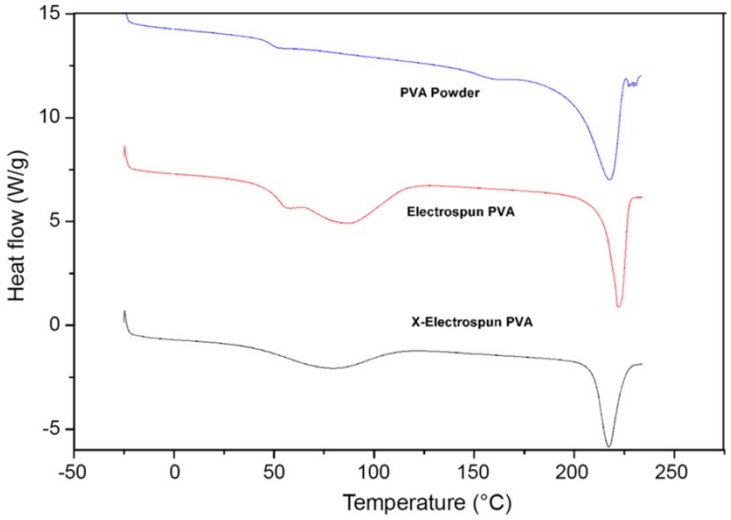

Figure S17 DSC curves of pure PVA samples (powder, fibers, and heattreated fibers).[23]

Enayati et al.[23] reported the DSC curves of PVA (powder, fibers, and heattreated fibers) (shown in Figure S17), which shows that the melting points of all are higher than 200 ℃. In the case of the powder and fibers, the DSC dynamic scans start with a change of specific heat which is the glass transition of PVA (around 50 °C). While for the heat treated electrospun material, there is no glass transition registered.

References

[1] E. A. Algaer, F. Müller-Plathe, *Soft Materials* **2012**, 10, 42.

[2] T. Terao, E. Lussetti, F. Müller-Plathe, *Physical Review E* **2007**, 75, 057701.

[3] P. L. Garrido, P. I. Hurtado, B. Nadrowski, *Physical Review Letters* **2001**, 86, 5486.

[4] J. Lange, F. G. de Souza, M. Nele, F. W. Tavares, I. S. V. Segtovich, G. C. Q. da Silva, J. C. Pinto, *Macromolecular Theory and Simulations* **2016**, 25, 45.

[5] N. Grønbech-Jensen, N. R. Hayre, O. Farago, *Computer Physics*

Communications **2014**, 185, 524.

[6] T. Schneider, E. Stoll, *Physical Review B* **1978**, 17, 1302.

[7] P. K. Schelling, S. R. Phillpot, P. Keblinski, *Physical Review B* **2002**, 65, 144306.

[8] L. T. Kong, *Computer Physics Communications* **2011**, 182, 2201.

[9] C. Campaná, M. H. Müser, *Physical Review B* **2006**, 74, 075420.

[10] L. T. Kong, G. Bartels, C. Campañá, C. Denniston, M. H. Müser, *Computer Physics Communications* **2009**, 180, 1004.

[11] X. Wang, M. Kaviany, B. Huang, *Nanoscale* **2017**, 9, 18022.

[12] S. D. Dabhi, P. K. Jha, *Polymer* **2015**, 81, 45.

[13] Pang, Y.; Yang, J.; Curtis, T. E.; Luo, S.; Huang, D.; Feng, Z.; Morales-Ferreiro, J. O.; Sapkota, P.; Lei, F.; Zhang, J.; Zhang, Q.; Lee, E.; Huang, Y.; Guo, R.; Ptasinska, S.; Roeder, R. K.; Luo, T. *ACS Nano* **2019**, 13 (2), 1097-1106.

[14] Loomis, J.; Ghasemi, H.; Huang, X.; Thoppey, N.; Wang, J.; Tong, J. K.; Xu, Y.; Li, X.; Lin, C.-T.; Chen, G. *TECHNOLOGY* **2014**, 02 (03), 189-199.

[15] Li, D.; Wang, Y.; Xia, Y. *Nano Letters* **2003**, 3 (8), 1167-1171.

[16] M. Deutsch, *Physical Review A* **1991**, 44, 8264.

[17] M. Xu, D. N. Futaba, M. Yumura, K. Hata, *Acs Nano* **2012**, 6, 5837.

[18] V. Casalegno, P. Vavassori, M. Valle, M. Ferraris, M. Salvo, G. Pintsuk, *Journal of Nuclear Materials* **2010**, 407, 83.

[19] W. Parker, R. Jenkins, C. Butler, G. Abbott, *Journal of applied physics* **1961**, 32, 1679.

[20] S. Seagle, K. Yu, S. Giangiordano, *Materials Science and Engineering: A* **1999**, 263, 237.

[21] A. Salazar, *European journal of physics* **2003**, 24, 351.

[22] J. P. Holman, *Experimental methods for engineers*, **2001**.

[23] M.S. Enayati, T. Behzad, P. Sajkiewicz., R. Bagheri, L. Ghasemi-Mobarakeh, W. Łojkowski, Z. Pahlevanneshan, M. Ahmadi, *Iranian Polymer Journal* **2016**, 25:647–659